

Steady and transient thermal stress analysis using a polygonal finite element method

Yang Yang^a, Mingjiao Yan^b, Zongliang Zhang^a, Xuedong Chen^a, Dengmiao Hao^b

^a*PowerChina Kunming Engineering Corporation Limited, Kunming, 650051, Yunnan, China*

^b*College of Water Conservancy and Hydropower Engineering, Hohai University, Nanjing, 210098, Jiangsu, China*

Abstract

While the finite element method (FEM) has been widely used for thermal stress problems, it faces challenges in handling complex geometries, non-matching meshes, and achieving computational efficiency. To address these limitations, this study proposes an N-sides finite element method (NS-FEM) for solving steady-state and transient thermal stress problems. By employing Wachspress basis functions for interpolation within polygonal elements, the method offers enhanced adaptability and accuracy in handling intricate boundary conditions and material properties. A series of numerical examples demonstrate the advantages of the proposed NS-FEM in terms of convergence, computational cost, and solution precision, as compared to conventional FEM. The results confirm the efficacy of NS-FEM in capturing detailed thermal and stress distributions, particularly in multi-scale and non-matching mesh scenarios. This work highlights the potential of NS-FEM as a robust approach for complex thermal stress analysis in engineering appli-

cations.

Keywords: Polygonal finite element method, thermal stress analysis, non-matching meshes, Wachspress basis functions

1. Introduction

Thermal stress analysis is a critical aspect of engineering and materials science, particularly in the design and evaluation of structures subjected to temperature variations [1]. As materials expand or contract due to thermal effects, stress can develop, potentially leading to structural failure if not adequately managed. Accurate modeling and analysis of thermal stresses are therefore essential for ensuring the reliability and safety of engineering systems [2]. The theory of thermo-elastic analysis is well-established, and analytical solutions can be obtained for some simple problems. However, due to the complexity of geometry and anisotropy, obtaining analytical solutions becomes challenging [3, 4].

Numerical approaches have become an alternatives technique to solve the problem of thermo-elasticity, such as the finite element method (FEM) [5, 6], the finite cell method (FCM) [7], the isogeometric analysis (IGA) [8, 9], the boundary element method (BEM) [10]. In particular, the FEM has long been a cornerstone in computational mechanics for solving a wide range of engineering problems [11, 12]. Traditional FEM approaches typically employ elements with a fixed number of sides, such as triangles or quadrilaterals in two dimensions [13]. While the FEM has proven effective, it often face chal-

lenges in handling complex geometries and ensuring computational efficiency.

The computational accuracy and reliability of the FEM are highly contingent on the quality of the elements utilized in the mesh [14]. To achieve greater precision, it is often necessary to employ high-quality meshes, which may require the implementation of complex re-meshing algorithms. In the context of large-scale problems, a frequently adopted approach is to apply a finer mesh in regions of particular interest [15, 16]. However, this practice can lead to mesh distortions at the interfaces between coarse and fine meshes, potentially compromising the validity of the solution in these transitional areas.

To address these challenges, the implementation of non-matching meshes provides increased flexibility in practice, as it allows for the utilization of varying mesh sizes across different domains [17, 18]. This method can result in notable enhancements in overall mesh quality. However, non-matching meshes can generate hanging nodes at the interfaces between adjacent elements of differing sizes. These hanging nodes can disrupt displacement compatibility between neighboring elements, potentially undermining the accuracy and convergence of numerical simulations [19].

To tackle the hanging nodes in non-conforming meshes, several methods have been introduced, such as the mortar segment-to-segment method [20], the multi-point constraint equations (MPC) [21], Arlequin method [22], penalty method [23]. To resolve the problem of hanging nodes, the polygonal FEM has been developed employed the approach of constructing polygons

to resolve the problem of hanging nodes, considering that these nodes can be treated as vertices of polygonal elements [24, 25]. This flexibility allows for more accurate meshing of complex geometries and can lead to improved solution accuracy and convergence properties. The NS-FEM extends the applicability of traditional FEM by offering enhanced geometric adaptability and potentially reducing the computational cost associated with meshing and solving complex problems.

This paper presents a comprehensive study on the application of the N-sides finite element method to thermal stress problems. We aim to demonstrate the efficacy of polygonal FEM in capturing the intricate stress distributions that arise due to thermal effects in various materials and structural configurations. Through a series of benchmark tests and practical applications, we will illustrate the advantages of NS-FEM over traditional FEM approaches in terms of accuracy, efficiency, and ease of implementation.

The structure of this paper is as follows: Section 2 provides a detailed overview of the theoretical foundation of NS-FEM, including its formulation and implementation. Section 3 outlines the methodology used for thermal stress analysis, including the governing equations and boundary conditions. Section 4 presents the results of numerical experiments, comparing NS-FEM with conventional FEM methods. Finally, Section 5 discusses the implications of our findings and concludes with potential future research directions in this field.

2. Thermal analysis

The governing equation of transient heat conduction in a two-dimensional (2D) solid body can be written as follows [26]:

$$\rho c \dot{\phi} - \nabla(\mathbf{k} \nabla \phi) - Q = 0, \quad (1)$$

where ϕ is the temperature, $\dot{\phi}$ is the temperature change rate, Q is the rate of internal heat generation, ρ is the density, c is the specific heat. The thermal conductivity, denoted as k , is expressed as:

$$k = \begin{bmatrix} k_x & 0 \\ 0 & k_y \end{bmatrix}. \quad (2)$$

With the initial conditions

$$\phi(x, y, t = 0) = \phi_0(x, y) \quad \text{in } \Omega, \quad (3)$$

and the boundary conditions

$$\phi(x, y) = \bar{\phi} \quad \text{in } S_1, \quad (4)$$

$$-k \frac{\partial \phi}{\partial n} = \bar{q}_n = q_2 \quad \text{on } S_2, \quad (5)$$

$$-k \frac{\partial \phi}{\partial n} = \bar{q}_n = g(\phi - \phi_\infty) \quad \text{on } S_3, \quad (6)$$

where ρ is the density, ϕ is the temperature, $\dot{\phi}$ is the temperature change rate, Ω is the computational domain, n is the outward normal vector to Ω . S is the boundary. Furthermore, $\bar{\phi}$ and q are the prescribed boundary temperature and heat flux, respectively. g is the convection heat transfer coefficient and ϕ_∞ is the ambient temperature.

The Galerkin weak form of the governing Eq. (1) and the boundary condition Eq. (4 ~ 6) can be expressed as:

$$\begin{aligned} & \int_{\Omega} \rho c \delta\phi^T \frac{\partial\phi}{\partial t} d\Omega + \int_{\Omega} (\nabla\delta\phi)^T k(\nabla\phi) d\Omega - \int_{\Omega} \delta\phi^T Q d\Omega \\ & + \int_{\Gamma_q} \delta\phi^T q d\Gamma + \int_{\Gamma_h} \delta\phi^T h(\phi - \phi_\infty) d\Gamma = 0 \end{aligned} \quad (7)$$

where ∇ denotes a differential operator defined as follows:

$$\nabla = \begin{bmatrix} \frac{\partial}{\partial x} \\ \frac{\partial}{\partial y} \end{bmatrix}. \quad (8)$$

In the Galerkin weak form given in Eq. (7), the temperature field ϕ can be approximated as:

$$\phi = \sum_{i=1}^m N_i \phi_i, \quad (9)$$

where ϕ_i represents the temperature at node i , and N_i is the corresponding shape function. By substituting Eq. (9) into Eq. (7), Eq. (7) can then be

expressed as:

$$\begin{aligned}
& \int_{\Omega} \rho c N^T N \frac{\partial \phi}{\partial t} d\Omega + \int_{\Omega} k \left[\frac{\partial N^T}{\partial x} \frac{\partial N}{\partial x} + \frac{\partial N^T}{\partial y} \frac{\partial N}{\partial y} \right] \phi d\Omega \\
& + \int_{\Gamma_2} N^T q d\Gamma + \int_{\Gamma_3} g N^T N \phi d\Gamma - g \int_{\Gamma_3} N^T T_a d\Gamma - \int_{\Omega} N^T Q d\Omega \\
& = \underbrace{\int_{\Omega} \rho c N^T N d\Omega}_{\mathbf{M}} \frac{\partial \phi}{\partial t} + \underbrace{\int_{\Omega} k \left[\frac{\partial N^T}{\partial x} \frac{\partial N}{\partial x} + \frac{\partial N^T}{\partial y} \frac{\partial N}{\partial y} \right] d\Omega}_{\mathbf{K}_h} \phi \\
& + \underbrace{\int_{\Gamma_3} g N^T N d\Gamma}_{\mathbf{K}_g} \phi + \underbrace{\int_{\Gamma_2} N^T q d\Gamma - g \int_{\Gamma_3} N^T T_a d\Gamma - \int_{\Omega} N^T Q d\Omega}_{\mathbf{Q}} = 0
\end{aligned} \tag{10}$$

The equilibrium equation of the discretized system can ultimately be written in the following matrix form:

$$\mathbf{M} \dot{\phi} + \underbrace{(\mathbf{K}_h + \mathbf{K}_g)}_{\mathbf{K}_{th}} \phi = \mathbf{Q}, \tag{11}$$

where \mathbf{K}_h and \mathbf{K}_g are the thermal stiffness matrix and thermal damping matrix, respectively.

In which

$$\mathbf{K}_h = k \int_{\Omega} \mathbf{B}_h^T \mathbf{B}_h d\Omega, \tag{12}$$

$$\mathbf{K}_g = \int_{\Gamma_3} g N^T N d\Gamma. \tag{13}$$

where \mathbf{B}_{th} , referred to as the "strain-thermal" matrix, is given by

$$\mathbf{B}_{th} = \nabla N = \begin{bmatrix} N_{i,x} \\ N_{i,y} \end{bmatrix}. \quad (14)$$

Eq. (15) also can be expressed as

$$\mathbf{M}_{th}\dot{\phi} + \mathbf{K}_{th}\phi = \mathbf{Q}, \quad (15)$$

where

$$\mathbf{M}_{th} = \rho c \int_{\Omega} N^T N d\Omega, \quad (16)$$

In this work, the backward difference method [27] is employed to solve Eq. (15). The time domain is discretized into several time steps, and the solution at each time node is progressively computed starting from the initial conditions. The nodal temperature at any intermediate time is then obtained through interpolation.

At time $[t, t + \Delta t]$, the temperature change rate $\dot{\phi}$ can be expressed as

$$\dot{\phi}(t) = \frac{\Delta\phi}{\Delta t} = \frac{\phi(t)^{t+\Delta t} - \phi(t)^t}{\Delta t}. \quad (17)$$

Eq. (17) is substituted into Eq. (15), and the equation at time step $t + \Delta t$ can be obtained as follows:

$$\left(\mathbf{K}_{th} + \frac{\mathbf{M}_{th}}{\Delta t}\right)\phi(t) = \mathbf{Q} + \left(\frac{\mathbf{M}_{th}}{\Delta t}\right)\phi(t - \Delta t). \quad (18)$$

3. Thermal mechanical analysis

The governing equation describing linear elasto-static behavior subjected to thermal load is expressed as

$$\sigma = \mathbf{D}(\varepsilon - \varepsilon_0), \quad (19)$$

where \mathbf{D} is the elastic matrix, and ε_0 represents the initial strain caused by the temperature variation ϕ . For 2D problems, the initial strain ε_0 is given by

$$\varepsilon_0 = \phi\beta \quad \text{plane stress}, \quad (20)$$

$$\varepsilon_0 = (1 + \nu)\phi\beta \quad \text{plane strain}, \quad (21)$$

with

$$\beta = [\alpha \quad \alpha \quad 0]^T, \quad (22)$$

where α and ν denote the coefficient of thermal expansion and Poisson's ratio, respectively. The thermal stress is incorporated as the initial stress σ_0 , expressed as:

$$\sigma_0 = \mathbf{D}\varepsilon_0. \quad (23)$$

When calculating thermal stresses, external loads such as body and surface forces are ignored. If present, the effects of these loads, including stress, can be superimposed using the principle of superposition. In the absence of such forces, the total potential energy of an elastic body is solely due to

strain energy, given by

$$\begin{aligned}
\Pi &= \frac{1}{2} \int_v (\varepsilon^e)^T \sigma dv \\
&= \frac{1}{2} \int_v (\varepsilon - \varepsilon_0)^T \mathbf{D} (\varepsilon - \varepsilon_0) dv \\
&= \frac{1}{2} \int_v \varepsilon^T \mathbf{D} \varepsilon dv - \int_v \varepsilon^T \mathbf{D} \varepsilon_0 dv + \frac{1}{2} \int_v \varepsilon_0^T \mathbf{D} \varepsilon_0 dv
\end{aligned} \tag{24}$$

After discretization, and considering that the third term does not affect the variation, it can be omitted. Thus, the above equation simplifies to:

$$\begin{aligned}
\Pi &= \frac{1}{2} \sum_e (\mathbf{a}^e)^T \int_{v^e} \mathbf{B}_{el}^T \mathbf{D} \mathbf{B}_{el} dv \mathbf{a}^e - \sum_e (\mathbf{a}^T) \int_{v^e} \mathbf{B}_{el}^T \mathbf{D} \varepsilon_0 dv \\
&= \frac{1}{2} \mathbf{a}^T \mathbf{K}_{el} \mathbf{a} - \mathbf{a}^T \mathbf{f}_{el}
\end{aligned} \tag{25}$$

where the matrix \mathbf{K}_{el} is the global stiffness matrix, given by:

$$\mathbf{K}_{el} = \int_{v^e} \mathbf{B}_{el}^T \mathbf{D} \mathbf{B}_{el} dv \tag{26}$$

Similarly, for the external forces due to initial strains, we can write:

$$\mathbf{f}_{el} = \int_{v^e} \mathbf{B}_{el}^T \mathbf{D} \varepsilon_0 dv \tag{27}$$

4. Polygonal element construction

Wachspress [28] introduced a class of rational basis functions for polygonal elements, founded on projective geometry principles. These functions are designed to achieve nodal interpolation and preserve boundary linearity by

employing the algebraic edge equations. Later, Warren [29, 30] extended Wachspress functions to support simplex convex polyhedra.

The procedure to construct these barycentric coordinates is as follows: let $R \subset \mathbb{P}^3$ be a simple convex polyhedron with its set of facets F and vertices V . For each facet $f \in F$, let \mathbf{n}_f represent the outward unit normal. Given a point $x \in P$, let $h_f(x)$ be the perpendicular distance from x to the facet f , expressed as:

$$h_f(\mathbf{x}) = (\mathbf{v} - \mathbf{x}) \cdot \mathbf{n}_f, \quad (28)$$

where $v \in V$ is a vertex of facet f . For a vertex v with incident facets f_1, f_2, f_3 , the weight function at any point $x \in P$ is defined as:

$$w_{\mathbf{v}}(\mathbf{x}) = \frac{\det(\mathbf{p}_{f_1}, \mathbf{p}_{f_2}, \mathbf{p}_{f_3})}{h_{f_1}(\mathbf{x})h_{f_2}(\mathbf{x})h_{f_3}(\mathbf{x})}, \quad (29)$$

where $\mathbf{p}_f(x) = \frac{\mathbf{n}_f}{h_f(x)}$ is the scaled normal vector to facet f , and f_1, f_2, \dots, f_d represent the d faces adjoining v , arranged counter-clockwise as seen from the exterior of P . The determinant \det is calculated over \mathbb{R}^d . The shape functions for a point $x \in P$ are then expressed as:

$$\phi_{\mathbf{v}}(\mathbf{x}) = \frac{w_{\mathbf{v}}(\mathbf{x})}{\sum_{\mathbf{u} \in V} w_{\mathbf{u}}(\mathbf{x})}. \quad (30)$$

This construction ensures that the shape functions $\phi_{\mathbf{v}}(\mathbf{x})$ interpolate nodal values and maintain boundary consistency across facets, offering a powerful basis for applications in polygonal finite element methods.

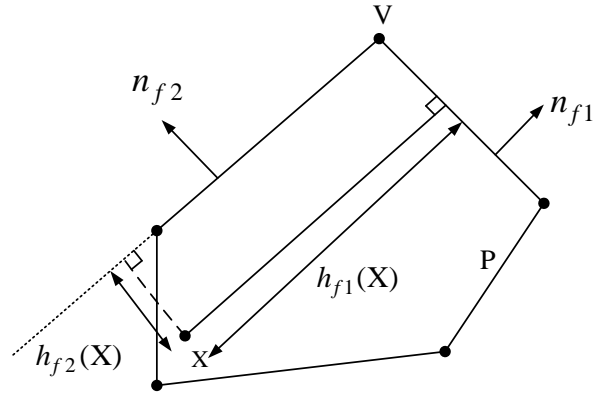


Fig. 1. Barycentric coordinates: Wachspress basis function.

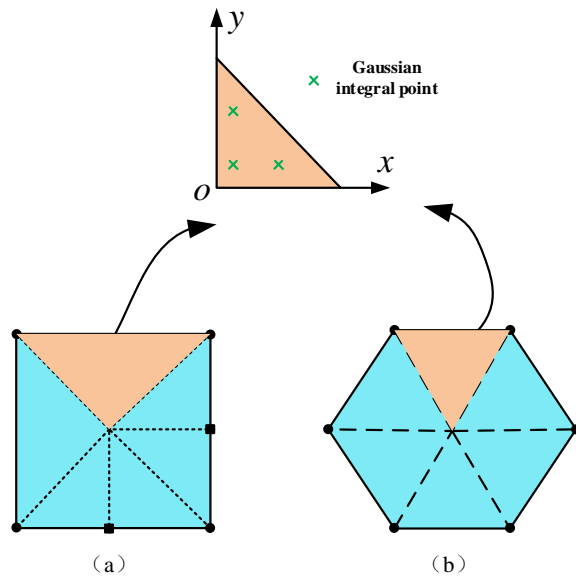


Fig. 2. Construction of the polygonal FEM element.

5. Implementation

5.1. Steady-state solutions

In this study, we only consider the effect of the temperature field on the displacement field, neglecting the influence of the displacement field on the temperature field. Hence, the thermal stress analysis focuses on the coupling between thermal and stress fields. The coupling equation can be expressed as:

$$\begin{bmatrix} \mathbf{K}_{\text{th}} & 0 \\ C_{el} & \mathbf{K}_{el} \end{bmatrix} \begin{Bmatrix} \phi \\ \mathbf{u} \end{Bmatrix} = \begin{Bmatrix} \mathbf{f}_{\text{th}} \\ \mathbf{f}_{el} \end{Bmatrix}, \quad (31)$$

where \mathbf{K}^{th} and \mathbf{K}^{el} denote the thermal and elastic stiffness matrices, respectively. The solution vector ϕ and \mathbf{u} are the temperature field and the displacement field, respectively. The vectors \mathbf{f}^{th} and \mathbf{f}^{el} denote the right-hand of the flux and force, respectively.

Eq. (31) can be solved as two steps. Firstly, we solve the temperature field as the following:

$$\mathbf{K}_{\text{th}}\phi = \mathbf{f}_{\text{th}}. \quad (32)$$

After obtaining the temperature field, the displacement field is then solved using the following equation:

$$\mathbf{K}_{el}\mathbf{u} = \mathbf{f}_{el} - C_{el}\phi. \quad (33)$$

5.2. Transient solutions

The coupling equation of transient thermal stress can be expressed as:

$$\begin{bmatrix} \mathbf{M}_{\text{th}} & 0 \\ 0 & 0 \end{bmatrix} \begin{Bmatrix} \dot{\phi} \\ \mathbf{u} \end{Bmatrix} + \begin{bmatrix} \mathbf{K}_{\text{th}} & 0 \\ \mathbf{C}_{el} & \mathbf{K}_{el} \end{bmatrix} \begin{Bmatrix} \phi \\ \mathbf{u} \end{Bmatrix} = \begin{Bmatrix} \mathbf{f}_{\text{th}} \\ \mathbf{f}_{el} \end{Bmatrix}, \quad (34)$$

where \mathbf{M}_{th} is the mass matrix of heat conduction, $\dot{\phi}$ is temperature change rate. At time $[t, t + \Delta t]$, the temperature change rate $\dot{\phi}$ can be expressed as

$$\dot{\phi}(t) = \frac{\Delta\phi}{\Delta t} = \frac{\phi(t + \Delta t) - \phi(t)}{\Delta t} \quad (35)$$

Similarly, Eq. (34) can also be solved in two steps: Firstly, we solve the temperature field ϕ of each moment as the following:

$$\mathbf{M}_{\text{th}}\dot{\phi} + \mathbf{K}_{\text{th}}\phi = \mathbf{f}_{\text{th}}. \quad (36)$$

Once the temperature field ϕ is determined, the displacement field is subsequently solved using the following equation:

$$\mathbf{K}_{el}\mathbf{u} = \mathbf{f}_{el} - \mathbf{C}_{el}\phi. \quad (37)$$

5.3. Implementation using ABAQUS UEL

In this work, we implemented thermal-stress analysis using ABAQUS with User-Defined Elements (UEL). Algorithm 1 presents a flowchart out-

lining the procedure for both steady-state and transient heat conduction analysis. The primary function of the UEL in ABAQUS is to update the element's contribution to the residual force vector (RHS) and the stiffness matrix (AMATRIX) through the user subroutine interface provided by the software. For steady state thermal stress analysis, the AMATRIX and RHS are defined as follows:

$$\text{AMATRIX} = \begin{bmatrix} \mathbf{K}_{\text{th}} & 0 \\ \mathbf{C}_{\text{el}} & \mathbf{K}_{\text{el}} \end{bmatrix}, \quad (38)$$

$$\text{RHS} = - \begin{bmatrix} \mathbf{K}_{\text{th}} & 0 \\ \mathbf{C}_{\text{el}} & \mathbf{K}_{\text{el}} \end{bmatrix} \begin{Bmatrix} \phi \\ \mathbf{u} \end{Bmatrix} + \begin{Bmatrix} \mathbf{f}_{\text{th}} \\ \mathbf{f}_{\text{el}} \end{Bmatrix}. \quad (39)$$

For transient thermal-stress analysis, the AMATRIX and RHS are defined as follows:

$$\text{AMATRIX} = \begin{bmatrix} \mathbf{K}_{\text{th}} & 0 \\ \mathbf{C}_{\text{el}} & \mathbf{K}_{\text{el}} \end{bmatrix}^{t+\Delta t} + \frac{1}{\Delta t} \begin{bmatrix} \mathbf{M}_{\text{th}} & 0 \\ 0 & 0 \end{bmatrix}^{t+\Delta t}, \quad (40)$$

$$\begin{aligned} \text{RHS} = & - \begin{bmatrix} \mathbf{K}_{\text{th}} & 0 \\ \mathbf{C}_{\text{el}} & \mathbf{K}_{\text{el}} \end{bmatrix}^{t+\Delta t} \begin{Bmatrix} \phi \\ \mathbf{u} \end{Bmatrix}^{t+\Delta t} \\ & - \frac{1}{\Delta t} \begin{bmatrix} \mathbf{M}_{\text{th}} & 0 \\ 0 & 0 \end{bmatrix}^{t+\Delta t} \left(\begin{Bmatrix} \phi \\ \mathbf{u} \end{Bmatrix}^{t+\Delta t} - \begin{Bmatrix} \phi \\ \mathbf{u} \end{Bmatrix}^t \right). \end{aligned} \quad (41)$$

Algorithm 1 Solving the thermal stress problems using the PFEM

Input: Nodes and elements information, material properties, and nodal temperatures ϕ_t and nodal displacements \mathbf{u}_t

Output: Nodal temperatures ϕ_{t+1} and nodal displacements \mathbf{u}_{t+1}

```

1: while ABAQUS not converged do
2:   Solve nodal temperatures  $\phi_{t+1}^k$  and nodal displacements  $\mathbf{u}_{t+1}^k$ 
3:   for 1 to AllEle do      !  Traverse all elements
4:     for 1 to Element subdomains do
5:       Construct triangular subdomains based on polygons
6:       Solve the subdomains of the stiffness  $\mathbf{K}_{el}^{sub}$  and  $\mathbf{K}_{th}^{sub}$  and mass
matrix  $\mathbf{M}_{th}^{sub}$ 
7:     end for
8:     Assemble the element stiffness  $\mathbf{K}_{el}$  and  $\mathbf{K}_{th}$  and mass matrix  $\mathbf{M}_{th}$ 
9:     if lflags(1)=71 then
10:      Update stiffness matrix AMATRIX and residual force vector
RHS using Eqs. (38) and (39)
11:    end if
12:    if lflags(1)=72 or lflags(1)=73 then
13:      Update stiffness matrix AMATRIX and residual force vector
RHS using Eqs. (39) and (41)
14:    end if
15:  end for
16:  update  $k = k + 1$ 
17:  Solve nodal temperatures  $\phi_{t+1} = \phi_{t+1}^k$  and nodal displacements
 $\mathbf{u}_{t+1} = \mathbf{u}_{t+1}^k$ 
18: end while

```

5.4. Defining the UEL elements

In this study, we employ polygonal and quadtree (hybrid quadtree) mesh discretization techniques for mesh partitioning, with the specific algorithm shown in Fig. 3. For detailed information on the mesh, please refer to the references [31, 32]. We will not elaborate on it further in this work.

Moreover, as illustrated in Fig. 4, we have developed a polygonal el-

ement, referred to as a “super element”, capable of supporting traditional elements, polygonal elements, and quadtree elements. The ABAQUS input file provides a comprehensive description of the numerical model, detailing nodes, elements, degrees of freedom, and material properties. For instance, as shown in Listing 1, the hexagonal element (U6) is defined as follows: Line 1 specifies the element type, the number of nodes, element properties, and degrees of freedom per node, while Line 2 defines the active degrees of freedom for displacement and temperature. Line 3 identifies the element type, and Line 4 outlines the node connectivity information. Other element types can be defined in a similar manner by following this structured approach.

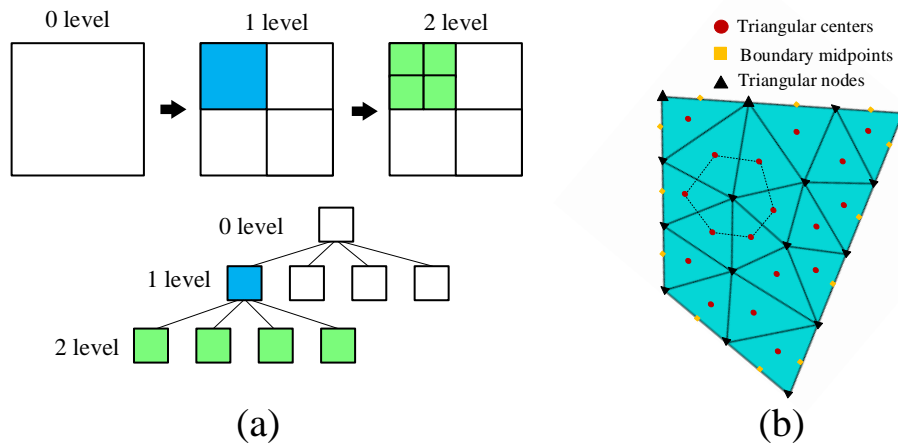


Fig. 3. Generation of a polygonal and quadtree meshes.

Listing 1: Input file of the polygon elements in UEL.

```

1 *USER ELEMENT, NODES=6, TYPE=U6, PROPERTIES=6, COORDINATES=2, VARIABLES=8
2 1, 2, 11

```

```

3 *Element,TYPE=U6
4 1, 1, 2, 3, 4, 5, 6
5 *USER ELEMENT,NODES=6,TYPE=U6,PROPERTIES=6,COORDINATES=2,VARIABLES=12
6 1,2,11
7 *Element,TYPE=U6
8 2, 7, 8, 9, 10, 11, 12, 13, 14

```

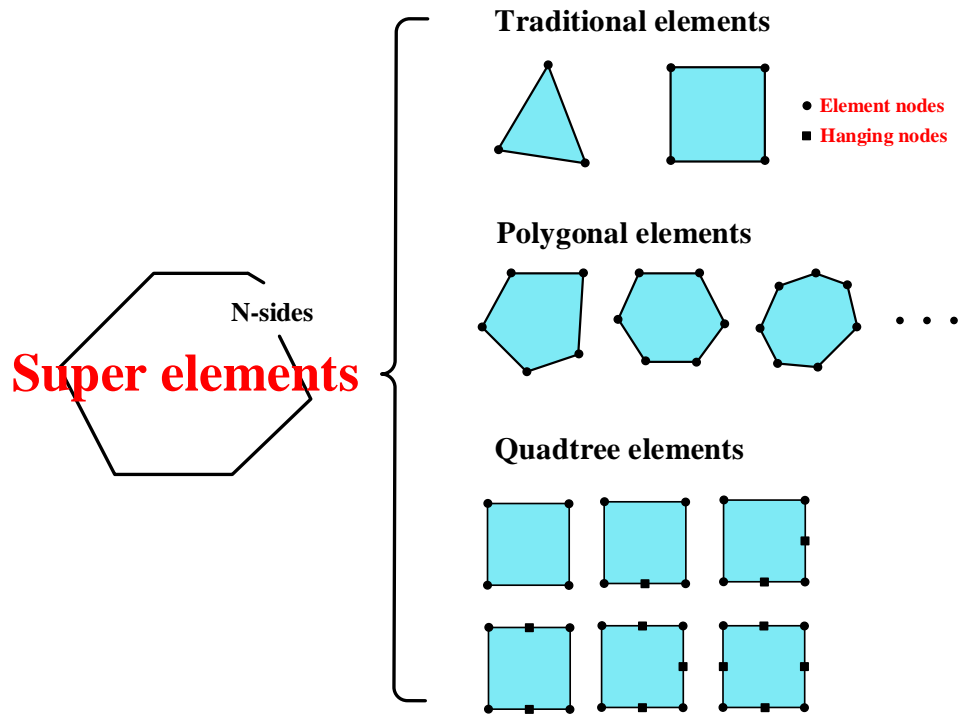


Fig. 4. Polygonal finite element support element types.

6. Numerical examples

This section presents four numerical benchmarks involving transient thermo-stress analysis. Additionally, the results of the proposed method are compared with those obtained from FEM. The FEM analysis uses the commercial finite element software ABAQUS. For validation, the relative error norm is investigated as follows:

$$\mathbf{e}_{L_2} = \frac{\|\mathbf{U}_{num} - \mathbf{U}_{ref}\|_{L_2}}{\|\mathbf{U}_{ref}\|_{L_2}}, \quad (42)$$

where \mathbf{U}_{num} is the numerical solution, and \mathbf{U}_{ref} is the analytical or reference solution. When exact solutions are not available for the presented numerical examples, the solutions obtained using the finite element commercial software ABAQUS are used as a reference.

6.1. Steady-state problem

6.1.1. Steady-state problem of a rectangular plate

In the first example, we consider a steady-state thermal stress problem of a rectangular plate, as shown in Fig. 5 (a). The length and high of the rectangular plate are 5 and 1, respectively. The left boundary is fixed ($U_x = 0, U_y = 0$). Moreover, the left and right boundaries are applied to the temperature 7 and 1, respectively. The material properties are considered as follows: $E=1.0, \nu=0, \alpha=1.0, k=1.0$, and $\rho c=1.0$.

The domain is discretized with polygonal elements, and a convergence study was conducted by refining the mesh through successive reductions in

element size, specifically 0.5, 0.25, 0.1, and 0.05. Moreover, to compare with the proposed method, the domain is discretized using quadrilateral elements (CPS4T) in ABAQUS. Element meshes with sizes of 0.25 and 0.1 are presented in Fig. 5 (b) and (c), respectively. Fig. 6 illustrated that the PFEM and FEM show a good convergence rate with the refining mesh. Moreover, the relative errors of the PFEM were smaller than those of the FEM for the same element size. The distributions of the temperature and displacement are illustrated in Fig. 7. Fig. 7 shows a good agreement in the temperature and displacement distribution between the reference solution and the PFEM solution.

Moreover, to demonstrate the capability of quadtree mesh discretization in multi-scale analysis, we discretized the beam using the quadtree mesh, as illustrated in Fig. 8. Figs. 8 (a) and (d) show the coarse mesh and fine mesh, respectively. Additionally, we refined the middle section of the beam, as shown in Figs. 8 (b) and (c). Tab. 1 summarizes the mesh properties and relative errors for the multi-scale meshes. Both multi-scale mesh 2 and the fine mesh achieved relative errors on the order of 10^{-5} , indicating excellent computational accuracy. Notably, the computational time for multi-scale mesh 2 was significantly shorter compared to the fine mesh. This highlights that multi-scale modeling, which focuses on refining the mesh in critical regions, can enhance accuracy while improving computational efficiency. Moreover, Fig. 9 demonstrates a strong agreement in temperature distribution between the reference solution and the FEM solution using the

quadtree mesh.

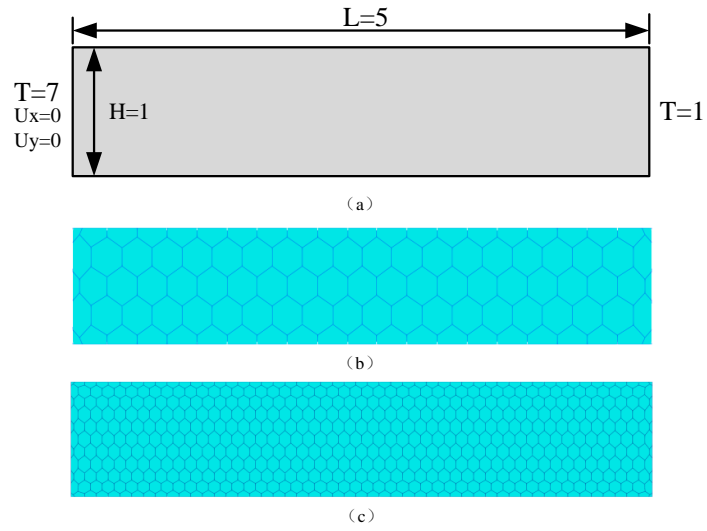


Fig. 5. Geometry and mesh model of the rectangular plate; (a) geometry and boundary conditions; (b) 0.25 mesh size; (c) 0.1 mesh size.

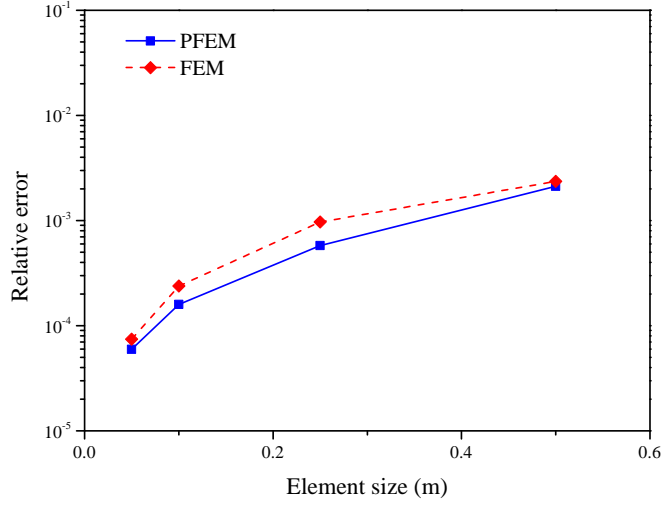


Fig. 6. Convergence of the relative error in the displacement.

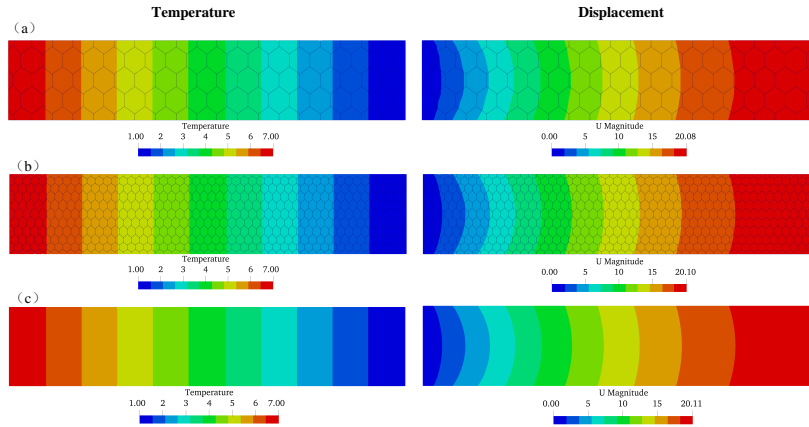


Fig. 7. Contours for temperature and displacement fields; (a) 0.25 mesh size; (b) 0.1 mesh size; (c) the reference solution.

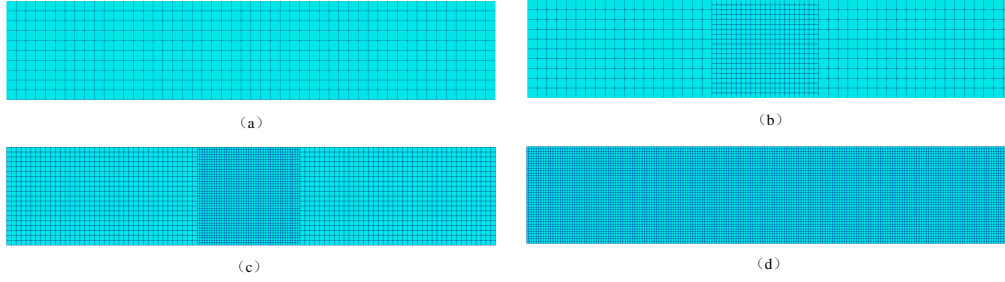


Fig. 8. Multi-scale model of the beam using the quadtree mesh; (a) coarse mesh; (b) multi-scale mesh 1; (c) multi-scale mesh; (d) fine mesh.

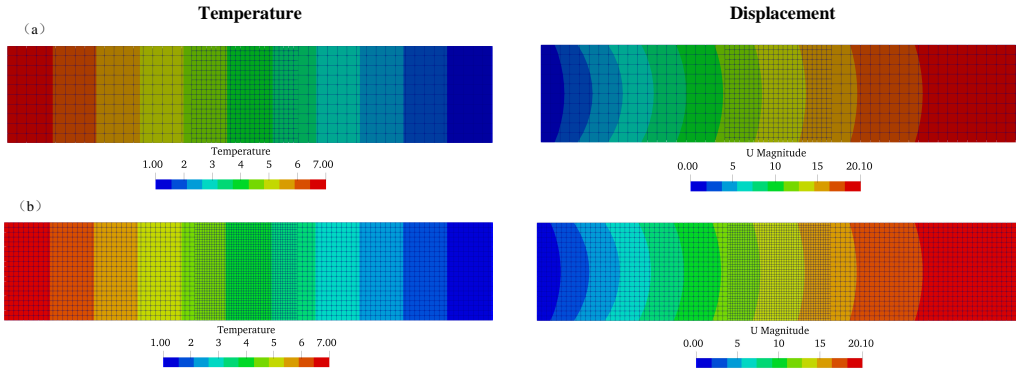


Fig. 9. Multi-scale model of the beam using the quadtree mesh; (a) coarse mesh; (b) multi-scale mesh 1; (c) multi-scale mesh; (d) fine mesh.

Tab. 1. Mesh characteristics and relative errors for the multi-scale meshes.

Mesh type	Elements	Nodes	Relative error	CPU time (s)
Coarse mesh	500	561	8.03×10^{-4}	0.40
Fine mesh	8000	8241	1.46×10^{-5}	6.70
Multi-scale mesh 1	810	912	1.09×10^{-4}	0.60
Multi-scale mesh 2	3220	3422	2.19×10^{-5}	2.80

6.1.2. 2D ring plate

In the first example, we investigate the thermo-electric state of the 2D ring plate, as shown in Fig. 10 (a). For this ring plate, the inner and outer radius are 0.25 and 1.0, respectively. The inner boundary is subjected to a displacement 0.25, and the outer boundary is fixed. Moreover, the inner and outer boundaries are applied to the temperature 3 and 1, respectively. The material properties are considered as follows: $E=1.0$, $\nu=0$, $\alpha=1.0$, $k=1.0$, and $\rho c=1.0$. The analytical solutions of the temperatures, displacement, and stress for this problems in cylindrical coordinates can be written as [33]

$$T_r(r) = 1 - \frac{\ln(r)}{\ln(2)}, \quad (43)$$

$$u_r(r) = -\frac{r \ln(r)}{2 \ln(2)}, \quad (44)$$

$$\sigma_r(r) = -1 + \frac{\ln(r) - 1}{2 \ln(2)}. \quad (45)$$

To verify the convergence and accuracy of the proposed method. The meshes following a sequence of element sizes: 0.1 m, 0.05 m, 0.025 m, and 0.0125 m. Figs. 10 (b) and (c) show the element meshes with an element size of 0.1 m. Fig. 12 shows that the PFEM's solutions in the radial direction for the 2D ring plate. It is noted that the solutions were close with the exact solutions, as shown in Fig. 11.

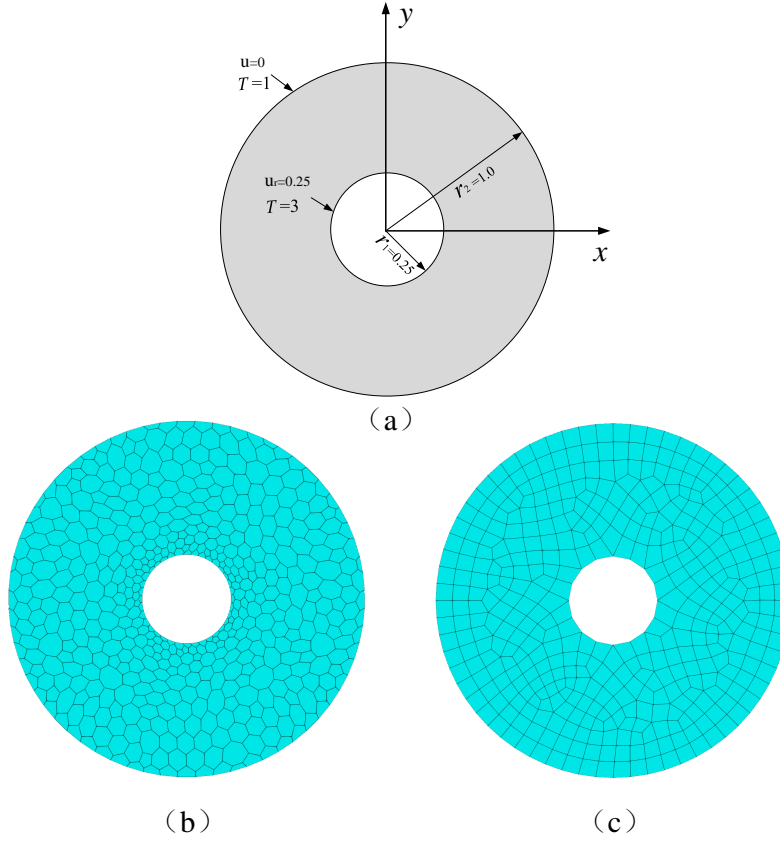


Fig. 10. The model of the 2D ring plate; (a) geometry and boundary conditions; (b) polygonal mesh at size 0.1 m; (c) quadrilateral mesh at size 0.1 m.

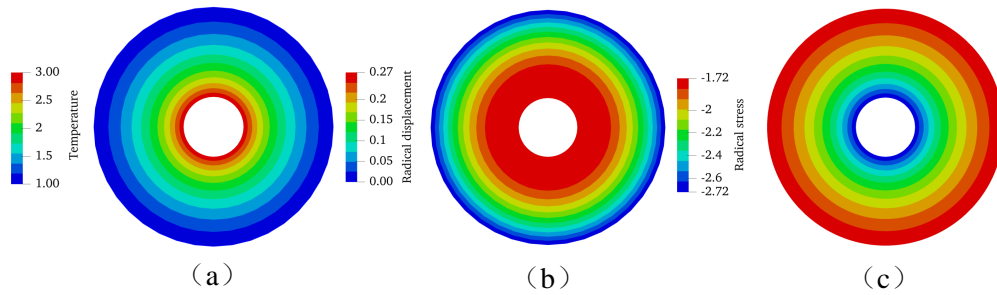


Fig. 11. Exact solutions in the radial direction for 2D ring plate; (a) temperature field; (b) radial displacement; (c) radial stress.

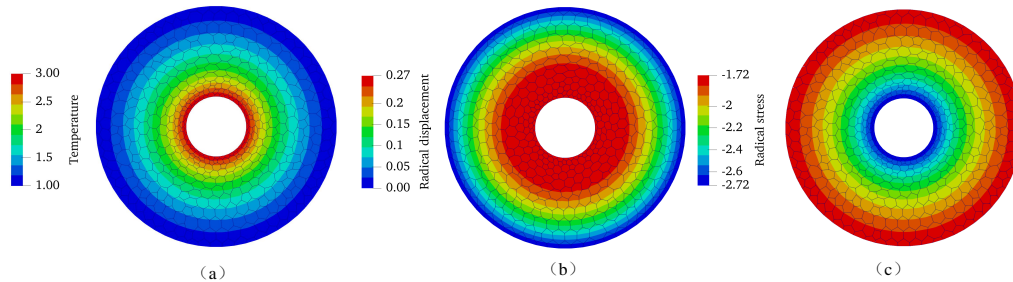


Fig. 12. PFEM solutions in the radial direction for 2D ring plate; (a) temperature field; (b) radial displacement; (c) radial stress.

6.2. Transient problems

6.2.1. L-shaped thin plate

In this example, we consider an L-shaped thin plate, as shown in Fig. 13. The bottom side is subjected to a fixed constraint, while a displacement of 0.1 m is applied to the top boundary. The right and top boundaries are subjected to temperatures of 500°C and 1000°C, respectively. The material properties used in the analysis are as follows: thermal conductivity of 3 W/m·°C, density of 2000 kg/m³, elastic modulus of 1×10^4 Pa, Poisson's ratio of 0.3, thermal expansion coefficient of 0.0011 °C⁻¹, and specific heat of 0.45 J/g·°C.

To verify the convergence and accuracy of PFEM for transient problems, the geometry is discretized using polygonal meshes with element sizes of 0.05 m, 0.025 m, and 0.001 m. A representative mesh is shown in Fig. 14. The total analysis time is set to 100 s, with a time step of 1 s. As shown in Fig. 15, both PFEM and FEM demonstrate good convergence rates, with PFEM achieving higher accuracy than FEM at the same element size. Furthermore,

Figs. 16 and 17 present the temperature and displacement histories at the monitoring point, obtained using PFEM and FEM, both of which align well with the reference solution. Finally, Fig. 18 depicts the distributions of temperature, displacement, and horizontal stress, where the PFEM results exhibit a high degree of consistency with the reference solution.

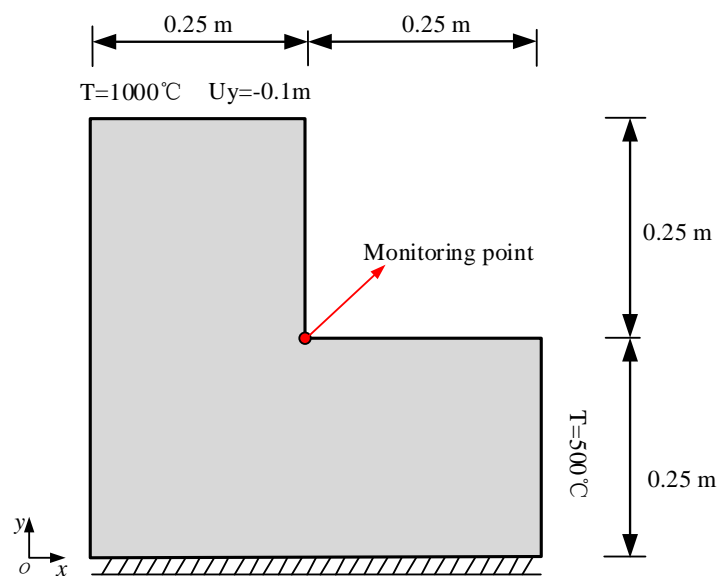


Fig. 13. Schematic diagram of a square body with multiple holes

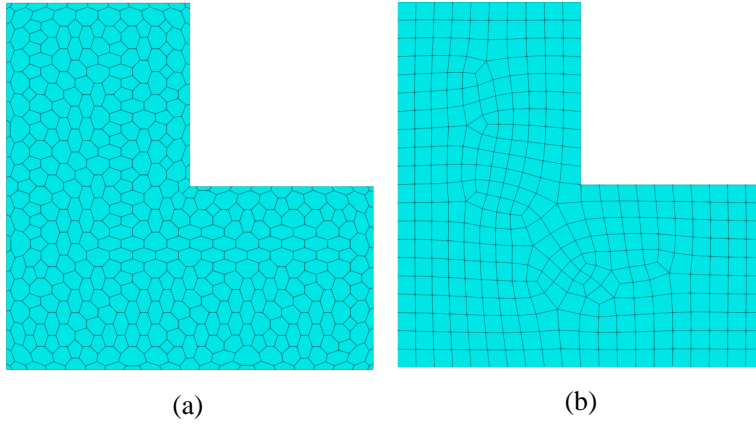


Fig. 14. Meshes of the L-shaped thin plate; (a) polygonal mesh; (b) quadrilateral mesh.

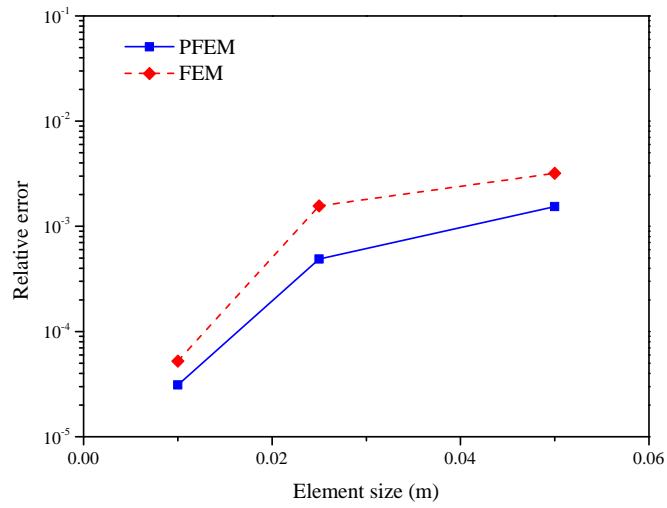


Fig. 15. Convergence of the relative error in the displacement.

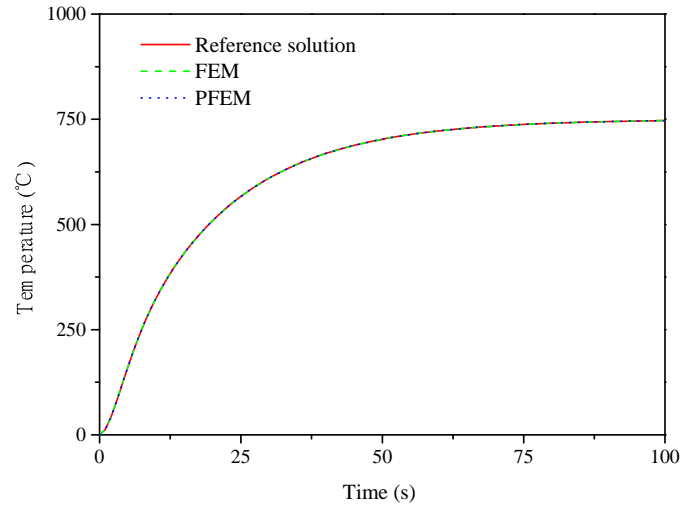


Fig. 16. Comparison of the PFEM and FEM in the history of temperature

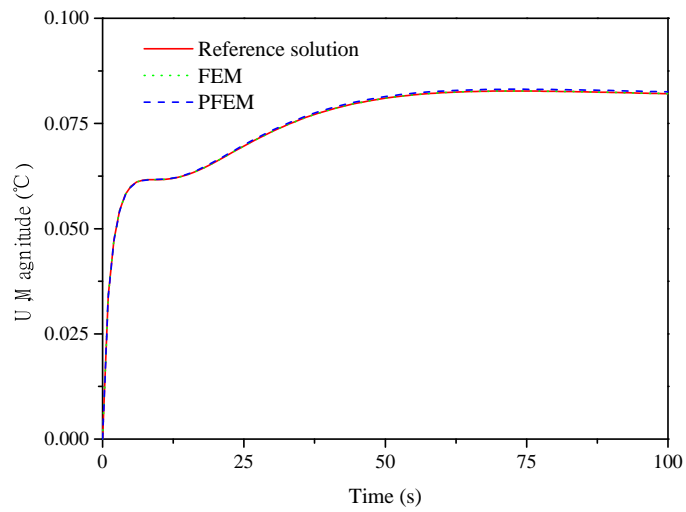


Fig. 17. Comparison of the PFEM and FEM in the history of displacement

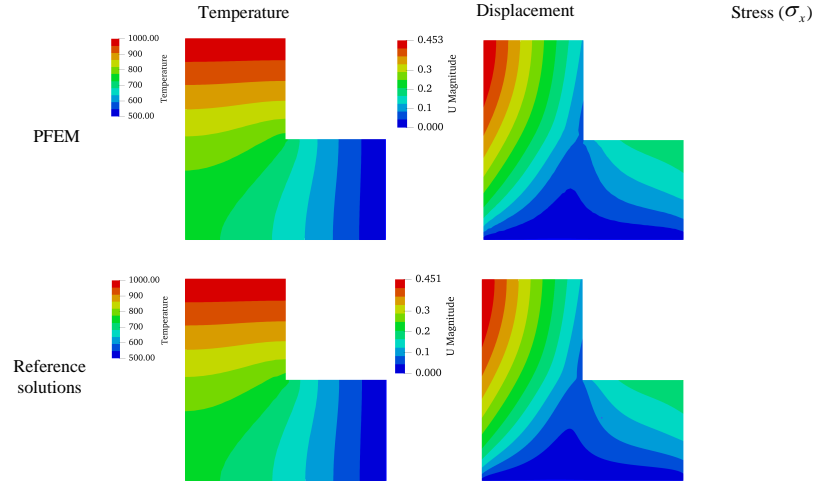


Fig. 18. Comparison of the PFEM and FEM in the history of displacement

6.2.2. Square panel with a complex cavity

To demonstrate the capability of the NS-FEM in solving transient thermal stress problems, a rectangular body (height $H = 2.0$ m, length $L = 1.0$ m) with a complex cavity, as shown in Fig. 19, is considered. The cavity is created by the intersection of four circles, each with a radius of 0.1 m. The bottom surface is maintained at 100°C , and the top surface is heated to 700°C . A displacement of 0.1 m is applied to the top surface. The material properties used in the analysis are: thermal conductivity $80 \text{ W/m}\cdot^\circ\text{C}$, density 3870 kg/m^3 , elastic modulus $1.2 \times 10^8 \text{ Pa}$, Poisson's ratio 0.3, thermal expansion coefficient $0.0011 \text{ }^\circ\text{C}^{-1}$, and specific heat $0.45 \text{ J/g}\cdot^\circ\text{C}$. The total analysis time is set to 50 s, with a time interval of 0.1 s.

In this example, the geometry is discretized using polygonal and hybrid quadtree meshing techniques, with an element size of 0.1 m, as shown in Fig.

20. The hybrid quadtree mesh, depicted in Fig. 20 (b), comprises regular quadtree elements for the simple regions and irregular polygonal elements (hybrid elements) for complex geometries. It is evident that the use of irregular polygonal elements allows the hybrid quadtree mesh to fit the boundary of the surface effectively. The temperature and displacement time history curves at monitoring points A and B are presented in Figs. 21 and 22, respectively. These results show good agreement with the reference solution. Additionally, as shown in Tab. 2, the relative error for the polygonal elements is lower than that of the hybrid quadtree elements, despite using the same element size. This is attributed to the increased number of nodes in the polygonal elements.

For improved accuracy at the monitoring points, local mesh refinement is applied to the region around the monitoring points, as illustrated in Fig. 19. The refined mesh is shown in Fig. 23. As indicated in Tab. 2, mesh refinement significantly reduces the computational error at the monitoring points. Furthermore, following refinement, the number of nodes in the polygonal elements is nearly identical to that in the refined hybrid quadtree mesh elements, yet the number of elements is reduced by 49.5%. Consequently, the computational time for the refined polygonal elements is shorter than that for the hybrid quadtree mesh.

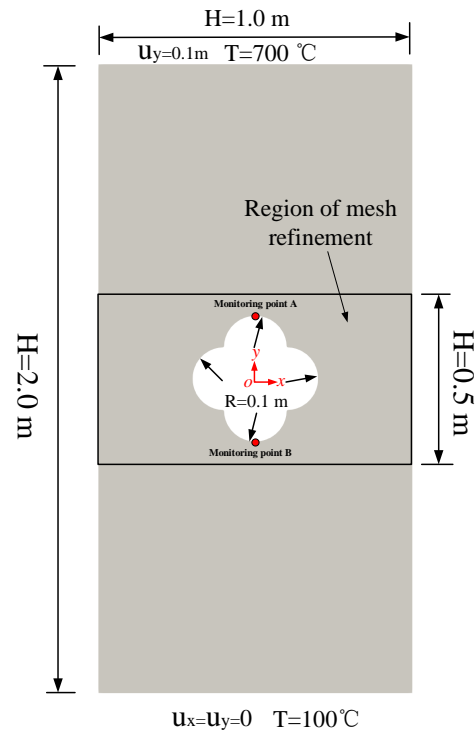


Fig. 19. Schematic diagram of a square body with multiple holes

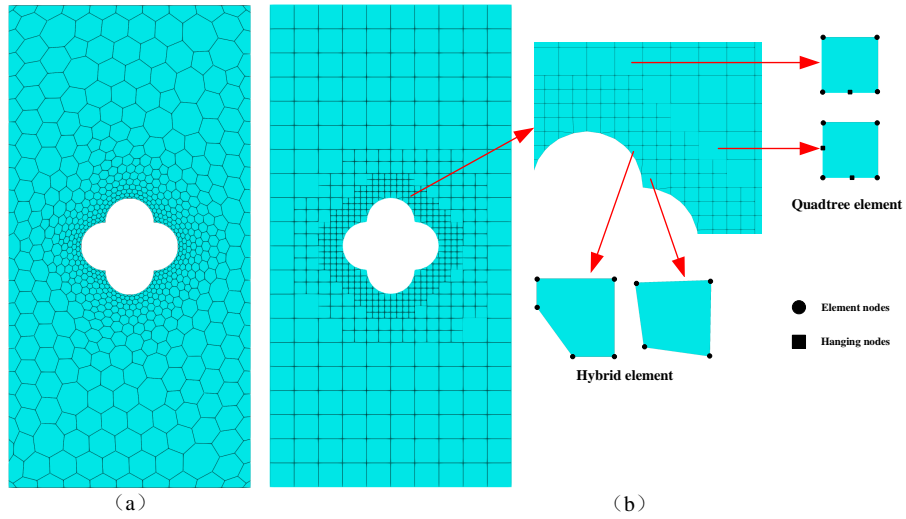


Fig. 20. Meshes of square panel; (a) polygonal mesh (b) hybrid mesh.

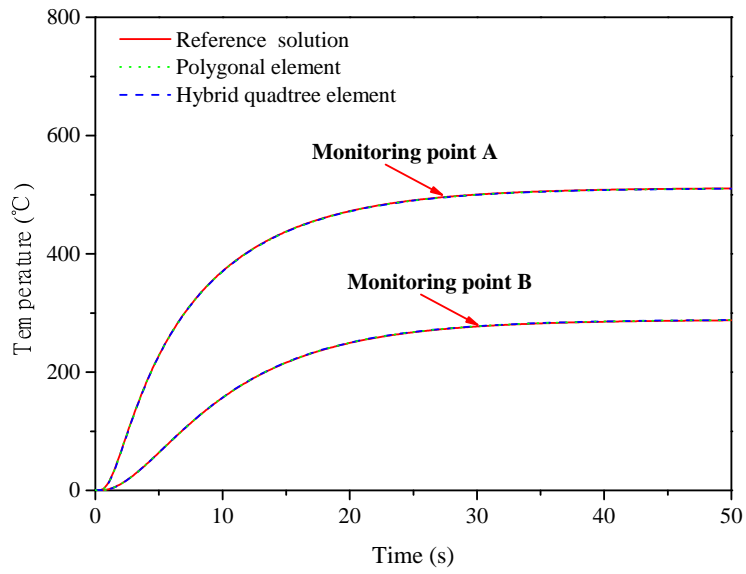


Fig. 21. Comparison of the polygonal element and hybrid quadtree element in the history of temperature.

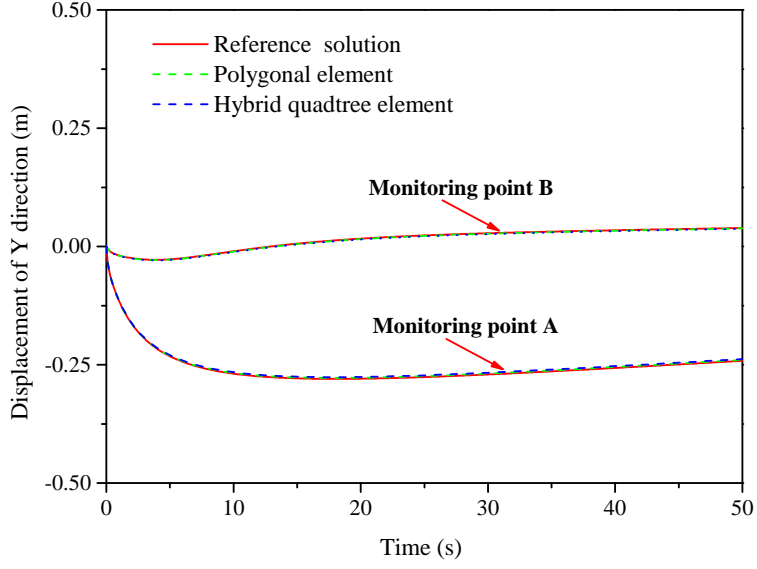


Fig. 22. Comparison of the polygonal element and hybrid quadtree element in the history of displacement.

Tab. 2. Relative errors for the monitoring points.

Element type	Elements	Nodes	Relative error for A	Relative error for B	CPU time (s)
Polygonal element	707	1422	8.21×10^{-4}	1.48×10^{-3}	179.30
Hybrid quadtree element	536	630	9.78×10^{-4}	1.87×10^{-3}	112.20
Refining polygonal element	5715	11438	2.49×10^{-4}	3.68×10^{-4}	1614.30
Refining hybrid quadtree element	11328	11664	3.09×10^{-4}	6.99×10^{-4}	2181.60

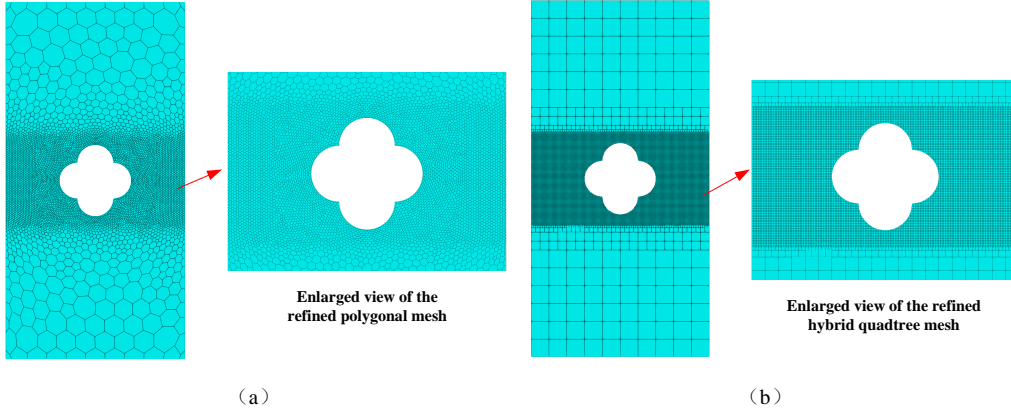


Fig. 23. Meshes of square panel; (a) polygonal mesh (b) hybrid mesh.

7. Conclusions

This study introduces an N-sides finite element method (NS-FEM) framework for addressing steady-state and transient thermal stress problems. By incorporating Wachspress basis functions for polygonal element interpolation, the proposed method effectively overcomes the limitations of conventional FEM in handling complex geometries, non-matching meshes, and multi-scale modeling. The main conclusions are summarized as follows:

(1) NS-FEM demonstrates excellent adaptability for complex geometries and boundary conditions, with its polygonal element interpolation mitigating issues associated with mesh incompatibility.

(2) Compared to traditional FEM, NS-FEM achieves superior convergence rates and computational efficiency, particularly in multi-scale modeling scenarios where computational precision and cost are balanced.

(3) Numerical examples validate the reliability and accuracy of NS-FEM

in predicting temperature fields and stress distributions, showing strong agreement with analytical and reference solutions.

Future research could focus on enhancing the performance of NS-FEM for higher-dimensional and nonlinear thermal conduction problems, as well as exploring its applications in real-world engineering contexts.

8. Acknowledgments

The Xing Dian Talent Support Program of Yunnan Province (grant NO. XDYC-QNRC-2022-0764) and the Yunan Fundamental Research Projects (grant NO. 202401CF070043) provided support for this study.

References

- [1] Q. Li, P. Hou, S. Shang, Accurate 3d thermal stress analysis of thermal barrier coatings, *International Journal of Mechanical Sciences* 217 (2022) 107024.
- [2] C. A. Moreira, G. B. Barbat, M. Cervera, M. Chiumenti, Accurate thermal-induced structural failure analysis under incompressible conditions, *Engineering Structures* 261 (2022) 114213.
- [3] S. Wu, G. Liu, X. Cui, T. Nguyen, G. Zhang, An edge-based smoothed point interpolation method (es-pim) for heat transfer analysis of rapid manufacturing system, *International Journal of Heat and Mass Transfer* 53 (9-10) (2010) 1938–1950.

- [4] M. Shibahara, S. Atluri, The meshless local petrov-galerkin method for the analysis of heat conduction due to a moving heat source, in welding, *International Journal of Thermal Sciences* 50 (6) (2011) 984–992. doi: <https://doi.org/10.1016/j.ijthermalsci.2010.12.012>.
- [5] Z. Luo, Y. Zhao, A survey of finite element analysis of temperature and thermal stress fields in powder bed fusion additive manufacturing, *Additive Manufacturing* 21 (2018) 318–332.
- [6] G. Giunta, G. De Pietro, H. Nasser, S. Belouettar, E. Carrera, M. Petrolo, A thermal stress finite element analysis of beam structures by hierarchical modelling, *Composites Part B: Engineering* 95 (2016) 179–195.
- [7] N. Zander, S. Kollmannsberger, M. Ruess, Z. Yosibash, E. Rank, The finite cell method for linear thermoelasticity, *Computers & Mathematics with Applications* 64 (11) (2012) 3527–3541.
- [8] N. Liu, P. A. Beata, A. E. Jeffers, A mixed isogeometric analysis and control volume approach for heat transfer analysis of nonuniformly heated plates, *Numerical Heat Transfer, Part B: Fundamentals* 75 (6) (2019) 347–362.
- [9] A. Gupta, A. Ghosh, Nurbs-based thermo-elastic analyses of laminated and sandwich composite plates, *Sādhanā* 44 (2019) 1–19.

- [10] C. Cheng, S. Ge, S. Yao, Z. Niu, Thermal stress singularity analysis for v-notches by natural boundary element method, *Applied Mathematical Modelling* 40 (19-20) (2016) 8552–8563.
- [11] M. Nemat-Alla, K. I. Ahmed, I. Hassab-Allah, Elastic–plastic analysis of two-dimensional functionally graded materials under thermal loading, *International Journal of solids and Structures* 46 (14-15) (2009) 2774–2786.
- [12] A. K. Faizin, R. Rizaldi, W. A. S. Putra, N. Hasan, Structural analysis of chassis frame of a prototype car: a finite element method, *Nusantara Science and Technology Proceedings* (2023) 252–256.
- [13] N. Ye, C. Su, Y. Yang, Free and forced vibration analysis in abaqus based on the polygonal scaled boundary finite element method, *Advances in Civil Engineering* 2021 (1) (2021) 7664870.
- [14] S. Li, X. Cui, N-sided polygonal smoothed finite element method (nsfem) with non-matching meshes and their applications for brittle fracture problems, *Computer Methods in Applied Mechanics and Engineering* 359 (2020) 112672.
- [15] H. D. Huynh, X. Zhuang, H. Nguyen-Xuan, A polytree-based adaptive scheme for modeling linear fracture mechanics using a coupled xfem–sbfem approach, *Engineering Analysis with Boundary Elements* 115 (2020) 72–85.

- [16] C. Jansari, K. Kannan, R. Annabattula, S. Natarajan, et al., Adaptive phase field method for quasi-static brittle fracture using a recovery based error indicator and quadtree decomposition, *Engineering Fracture Mechanics* 220 (2019) 106599.
- [17] L. A. Bitencourt Jr, O. L. Manzoli, P. G. Prazeres, E. A. Rodrigues, T. N. Bittencourt, A coupling technique for non-matching finite element meshes, *Computer methods in applied mechanics and engineering* 290 (2015) 19–44.
- [18] O. Manzoli, E. Rodrigues, L. Bitencourt, T. Bittencourt, M. Sánchez, An adaptive concurrent two-scale fe model to predicting crack propagation in concrete, in: *Computational Modelling of Concrete Structures*, CRC Press, 2018, pp. 127–136.
- [19] M. Yan, Y. Yang, Z. Zhang, C. Su, T. Luo, A psbfem approach for solving seepage problems based on the pixel quadtree mesh, *Geofluids* 2023 (1) (2023) 9092488.
- [20] M. A. Puso, T. A. Laursen, A mortar segment-to-segment frictional contact method for large deformations, *Computer methods in applied mechanics and engineering* 193 (45-47) (2004) 4891–4913.
- [21] L. Jendele, J. Červenka, On the solution of multi-point constraints—application to fe analysis of reinforced concrete structures, *Computers & Structures* 87 (15-16) (2009) 970–980.

- [22] W. Sun, S. Bao, J. Zhou, P. Ni, Concurrent multiscale analysis of anti-seepage structures in embankment dam based on the nonlinear arlequin method, *Engineering Analysis with Boundary Elements* 149 (2023) 231–247.
- [23] A. Pantano, R. C. Averill, A penalty-based interface technology for coupling independently modeled 3d finite element meshes, *Finite elements in analysis and design* 43 (4) (2007) 271–286.
- [24] A. Rajagopal, M. Kraus, P. Steinmann, Hyperelastic analysis based on a polygonal finite element method, *Mechanics of Advanced Materials and Structures* 25 (11) (2018) 930–942.
- [25] A. Tabarraei, N. Sukumar, Extended finite element method on polygonal and quadtree meshes, *Computer Methods in Applied Mechanics and Engineering* 197 (5) (2008) 425–438.
- [26] F. Li, P. Ren, A novel solution for heat conduction problems by extending scaled boundary finite element method, *International Journal of Heat and Mass Transfer* 95 (2016) 678–688.
- [27] O. C. Zienkiewicz, R. L. Taylor, *The finite element method: solid mechanics*, Vol. 2, Butterworth-heinemann, 2000.
- [28] E. L. Wachspress, A rational basis for function approximation, in: *Conference on Applications of Numerical Analysis: Held in Dundee/Scotland*, March 23–26, 1971, Springer, 2006, pp. 223–252.

- [29] J. Warren, On the uniqueness of barycentric coordinates, *Contemporary Mathematics* 334 (2003) 93–100.
- [30] J. Warren, S. Schaefer, A. N. Hirani, M. Desbrun, Barycentric coordinates for convex sets, *Advances in computational mathematics* 27 (2007) 319–338.
- [31] N. Ye, C. Su, Y. Yang, PSBFEM-Abaqus: Development of User Element Subroutine (UEL) for Polygonal Scaled Boundary Finite Element Method in Abaqus, *Mathematical Problems in Engineering* 2021 (2021) 1–22. doi:10.1155/2021/6628837.
- [32] M. Yan, Y. Yang, C. Su, Z. Zhang, Q. Duan, J. Luo, G. Xiong, T. Luo, A fast cell-smoothed finite element method for solving static–dynamic problems using a hybrid quadtree mesh, *International Journal of Computational Methods* (2024) 2450071.
- [33] P. Li, G. Lin, J. Liu, Y. Zhou, B. Xu, Solution of steady-state thermoelastic problems using a scaled boundary representation based on nonuniform rational b-splines, *Journal of Thermal Stresses* 41 (2) (2018) 222–246.